Bi-chromatic emission and multi-mode dynamics in bidirectional Ring Lasers

Antonio Pérez-Serrano
*Instituto de Física Interdisciplinar y Sistemas Complejos, IFISC, UIB-CSIC, Campus UIB, Palma de Mallorca, E-07122, Spain.**

Julien Javaloyes
Dept. of Electronics and Electrical Engineering, University of Glasgow, Glasgow, G12 8LT, UK.

Salvador Balle
Institut Mediterrani d'Estudis Avançats, IMEDEA, UIB-CSIC, Esporles, E-07190, Spain.
(Dated: October 9, 2009)

The multi-mode dynamics of a two-level ring laser is explored numerically using a bidirectional Travelling Wave Model retaining the spatial effects due to the presence of counter-propagating electric fields in the population inversion. Novel dynamical regimes where the emission in each direction occurs at different wavelength are studied. Mode-locked unidirectional emission for large gain bandwidth and relatively small detuning is reported.

I. INTRODUCTION

Since their inception, Ring Lasers (RLs) have attracted the interest of both theoretical and experimental research. From the theoretical point of view, the RL design offers the possibility of unidirectional operation due to their rotational symmetry which presents a very low —ideally vanishing— coupling of waves propagating in one direction and the opposite. Moreover, the RL design opens the possibility of tailoring the reversibility of the optical paths. This allows to more efficiently extract power from these devices, hence the unidirectional RL design is at the heart of many high-power solid state and fiber lasers [1]-[3] which are commonplace in many applications.

The reversibility of the optical path in RLs also allows for the coexistence of counter-propagating electric fields in the same gain medium, which leads to a large variety of operating regimes and dynamics that are profoundly different from those of Fabry-Pérot lasers [4]-[8]. Such a property has immediate potential applications for RLs acting as gyroscopes [9]. Moreover, the coexistence of counter-propagating waves can also be exploited for all-optical signal processing and storage via their directional bistability [10].

The first systematic formulation of the theory of a RL was proposed by Lamb et al. [11]-[13] in the early years of laser physics and relies on a derivation of the electromagnetic field equations in a semi-classical framework. This work contained the first qualitative analysis of travelling wave modes in a polygonal cavity, and was focused on a gas (He-Ne) active medium embedded in a Michelson polygonal resonator. The work by Lamb, though specific for gas lasers, already evidenced that each longitudinal mode showed a twofold degeneracy. Moreover, Lamb's work highlighted that symmetry issues and intra-cavity reflections have a major impact on the modal structure in ring lasers; and that pure counter-propagating travelling waves are ideal states only allowed in closed loop optical cavities without any localized reflection. Detuned standing waves better fit a close loop optical cavity with localized reflections, because they adjust nodes and maxima of the field intensity according to these special points along the cavity.

RLs are often modeled by Rate Equations (RE) ([5], [14]-[16]) for both unidirectional and bidirectional cases for different laser types. These models usually describe the electric fields and the population difference without taking into account the spatial effects explicitly. A natural way to take into account the spatial effects and describe multi-mode dynamics is to use a Travelling Wave Model (TWM). Such description offers a comprehensive model, but adds a bigger computational cost, because RE models are based in systems of Ordinary Differential Equations (ODEs) and a TWM description is based in systems of Partial Differential Equations (PDEs). A TWM description was already used for Fabry-Pérot lasers [17], [18], for unidirectional RLs [19] and even for bidirectional RLs [20]. Although this description for RL is not new, the novelty presented in this paper is the study of multi-mode dynamics.

The model here derived is a semi-classical model where the fields are described classically while the active medium is quantized. Since our goal is to formulate a description of the ring laser allowing for bidirectional emission and mode competition that retains the essential features of the dynamics, we consider the active medium be simply composed of two-level atoms. In this case, the interaction of the active medium and the optical field is well known and its description in time domain poses no additional problems as it would be the case for e. g. semiconductor systems. In addition, although a complete description of the system requires the full three-dimensional wave equation to describe the cavity field exactly, our approach only takes into account the axial

*Electronic address: antonio@ifisc.uib-csic.es

direction of propagation by assuming a single-transverse mode be supported by the cavity.

The paper is organized as follows. In Section II, the TWM is presented and analytical and quasi-analytical results are shown. In Section III, the test performed to assure the correctness and accuracy of the numerical algorithm used to implement the TWM is presented. In Section IV, the multi-mode dynamics of the system are discussed, focussing in two cases: moderate and large gain bandwidth. Finally, the conclusions are written in Section V. Moreover we include the detailed derivation of the model and its numerical implementation in appendix form.

II. THE MODEL

In this section we briefly summarize the TWM considered for the ring laser. The details of its derivation can be found in appendix A.

We consider that the electric field is quasi-monochromatic and it is decomposed into forward (+) and backward (-) waves propagating in opposite directions. The active medium is assumed to be composed by homogeneously broadened two level atoms. We also consider a quasi-resonant light matter interaction in the Rotating Wave Approximation (RWA). The population inversion density, D, is decomposed in different spatial harmonics of a fundamental modulation at half the optical wavelength and, in the resulting hierarchy of contributions, we retain the first order term.

With these assumptions, the dimensionless equations that define the TWM read

$$\pm\frac{\partial A_\pm}{\partial s} + \frac{\partial A_\pm}{\partial \tau} = B_\pm - \alpha A_\pm \,, \tag{1}$$

$$\begin{aligned}\frac{1}{\gamma}\frac{\partial B_\pm}{\partial \tau} &= -(1+i\widetilde{\delta})B_\pm + g(D_0 A_\pm + D_{\pm 2}A_\mp) \\ &+ \sqrt{\beta D_0}\;\xi_\pm(s,\tau)\,,\end{aligned} \tag{2}$$

$$\begin{aligned}\frac{1}{\epsilon}\frac{\partial D_0}{\partial \tau} &= J - D_0 + \Delta\frac{\partial^2 D_0}{\partial s^2} \\ &- (A_+B_+^* + A_-B_-^* + c.c.),\end{aligned} \tag{3}$$

$$\frac{1}{\eta}\frac{\partial D_{\pm 2}}{\partial \tau} = -D_{\pm 2} - \frac{\epsilon}{\eta}(A_\pm B_\mp^* + A_\mp^* B_\pm)\,, \tag{4}$$

where $A_\pm$ are the slowly varying components of the counter-propagating electric fields, $B_\pm$ are their respective polarizations, D_0 is the quasi-homogeneous inversion density and $D_{\pm 2}$ are the spatially-dependent contributions to the grating in the population inversion density, α are the internal losses, and $\widetilde{\delta}$ is the detuning, ϵ and η are the decay times for D_0 and $D_{\pm 2}$ respectively, and γ determines the spectral width of the gain spectrum. The space s is normalized to the cavity length L, $s = z/L$, and the time τ is normalized to a single round trip, $\tau = t/(L/v)$, where v is the group velocity. We note at this point that the mode spacing is 2π for a ring and π for a FP. For more details see appendix A.

Equations (1-4) must be completed with the boundary conditions for the electric fields. We consider the most general case depicted in Fig. 1, hence the boundary conditions read

$$\begin{aligned}A_+(0) &= t_+ A_+(1)e^{i\gamma\widetilde{\omega}_0} + r_- A_-(0), \\ A_-(1)e^{-i\gamma\widetilde{\omega}_0} &= t_- A_-(0) + r_+ A_+(1)e^{i\gamma\widetilde{\omega}_0},\end{aligned} \tag{5}$$

where $r_\pm$ and $t_\pm$ denote the reflectivity and transmissivity of the forward and backward waves. These coefficients can in general be different for the two directions in order to describe the effect of non-reciprocal elements as an optical isolator. We note moreover that $|t_\pm|^2 + |r_\pm|^2 = 1 - \varepsilon_\pm$, where $\varepsilon_\pm$ are the losses at the point coupler.

These general boundary conditions reduce to those for an ideal ring if $r_\pm = 0$ and $t_\pm \neq 0$, and to those for a Fabry-Pérot cavity if $r_\pm \neq 0$ and $t_\pm = 0$. When $r_+ = r_-$ and $t_+ = t_-$ the device is symmetrical for the two propagation directions.

In the following we shall take $\gamma\widetilde{\omega}_0 = 2\pi m$ where $m = 0, \pm 1, \pm 2 \ldots$ then $e^{i\gamma\widetilde{\omega}_0} = 1$ without loss of generality: it simply means that we take as the carrier frequency ω_0 that corresponding to one of the modes of the cavity. Moreover, we shall restrict ourselves to symmetric devices unless explicitly noted.

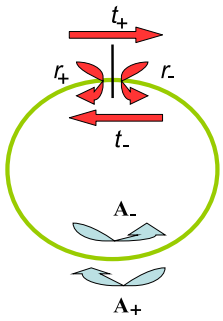

FIG. 1: Schematic representation of the ring laser boundary conditions where $t_\pm$ and $r_\pm$ are the the reflectivity and transmissivity for the counter-propagating fields $A+$ and A_- respectively.

A. Laser Threshold

The lasing threshold of the system can be readily determined by performing the linear stability analysis (LSA) around the off solution, i.e. $A_\pm^{st} = 0$, $B_\pm^{st} = 0$, $D_{\pm 2}^{st} = 0$ and $D_0^{st} = J$. We linearize (1-4) around this solution by introducing the small perturbations

$$\begin{aligned}A_\pm &= \varepsilon\; a_\pm(s,\tau), \qquad B_\pm = \varepsilon\; b_\pm(s,\tau), \\ D_0 &= J + \varepsilon^2\; d_0(s,\tau), \quad D_{\pm 2} = \varepsilon^2\; d_{\pm 2}(s,\tau).\end{aligned} \tag{6}$$

Where ε is infinitesimally small, then retaining the terms to first order in ε and assuming that the perturbations

evolve in time as

$$a_\pm(s,\tau) = \widetilde{a}_\pm(s)e^{\lambda\tau},\ \ b_\pm(s,\tau) = \widetilde{b}_\pm(s)e^{\lambda\tau}, \qquad (7)$$

we can obtain the eigenvalues λ_m $(m = 0, \pm1, \pm2, ...)$ whose real part determines whether or not the mode m is stable and whose imaginary part determines the modal frequency. The modal threshold is thus given by the current value J_m^{th} such that $Re(\lambda_m) = 0$. In our case, we obtain two different branches of solutions ($\sigma = \pm1$) whose modal thresholds read

$$J_m^{th}(\sigma) = \frac{(\gamma\widetilde{\delta} - 2\pi m)^2(\alpha - \ln(t+\sigma r))}{g(\alpha+\gamma-\ln(t+\sigma r))^2} - \frac{1}{g}\ln(t+\sigma r), \qquad (8)$$

and which have modal frequencies

$$\Omega_m(\sigma) = \frac{2\pi m + \widetilde{\delta}(\alpha - \ln(t+\sigma r))}{1+\frac{1}{\gamma}(\alpha-\ln(t+\sigma r))}. \qquad (9)$$

The thresholds for the two branches of solutions are shown in Fig. 2 for typical ring laser parameters. For small modal index, the lorentzian can be approximated by a parabola, which explains the shape of Fig. 2, and the minimum threshold corresponds to the gain peak. The two branches of solutions arise from the non-vanishing reflectivity r: when $r = 0$, the modes are pure forward and backward waves which are degenerate; however, for $r \neq 0$ the rotational invariance of the system is broken and the modes are given by combinations of the forward and backward waves that lift this degeneracy in both frequency and threshold gain. For $r \to 0$, eqs. (8) and (9) read

$$\begin{aligned} J_m^{th}(\sigma) &= \frac{(\gamma\widetilde{\delta}-2\pi m)^2(\alpha-\ln t)}{g(\alpha+\gamma-\ln t)^2} - \frac{1}{g}\ln t \\ &+ \frac{\sigma(\gamma\widetilde{\delta}-2\pi m)^2(\alpha-\gamma-\ln t)}{gt(\alpha+\gamma-\ln t)^3} r + O(r)^2 \end{aligned} \qquad (10)$$

and

$$\begin{aligned} \Omega_m(\sigma) &= \frac{\gamma[2\pi m+\widetilde{\delta}(\alpha-\ln t)]}{\alpha+\gamma-\ln t} \\ &+ \frac{\gamma\sigma(2\pi m-\gamma\delta)}{t(\alpha+\gamma-\ln t)^2} r + O(r)^2. \end{aligned} \qquad (11)$$

Such an effect has been experimentally observed in semiconductor ring lasers [21] where the residual reflectivities in the laser cavity induced modal doublets that correspond to the mode-pulling formula (9). The threshold difference for these doublets is roughly proportional to r for small reflectivities hence the gain difference can be hardly noticeable specially for appreciable internal losses α.

B. Monochromatic Solutions

The nontrivial monochromatic solutions read

$$\begin{aligned} A_\pm = A_\pm^{st}e^{-i\widetilde{\omega}\tau},\ \ B_\pm = B_\pm^{st}e^{-i\widetilde{\omega}\tau}, \\ D_0 = D_0^{st},\qquad D_{\pm2} = D_{\pm2}^{st}. \end{aligned} \qquad (12)$$

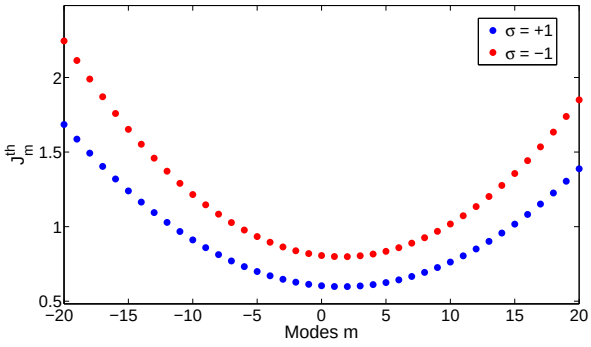

FIG. 2: J_m^{th} vs m. $\widetilde{\delta} = 0.1$, $g = 1$, $t = 0.5$, $r = 0.05$, $\alpha = 0$ and $\gamma = 100$. In this case the lowest threshold corresponds to mode $m = 2$ with $J_2^{th} = 0.5981$ for $\sigma = +1$.

where $\widetilde{\omega}$ is the lasing frequency. We use (12) in (1-4) finding

$$\pm\frac{\partial A_\pm^{st}}{\partial s} + (\alpha - i\widetilde{\omega})A_\pm^{st} = B_\pm^{st}\,, \qquad (13)$$

$$B_\pm^{st} = \frac{g(D_0^{st}A_\pm^{st} + D_{\pm2}^{st}A_\mp^{st})}{1+i(\widetilde{\delta}-\widetilde{\omega}/\gamma)}\,, \qquad (14)$$

$$D_0^{st} = J - (A_+^{st}B_+^{st*} + A_-^{st}B_-^{st*} + c.c.)\,, \qquad (15)$$

$$D_{\pm2}^{st} = -\frac{\epsilon}{\eta}(A_\pm^{st}B_\mp^{st*} + A_\mp^{st*}B_\pm^{st})\,. \qquad (16)$$

Analytical solutions for these equations can be found only in the simplest situation $r = 0$ and $\alpha = 0$. In this limit, the two counter-propagating waves are degenerate and a bidirectional solution also exists. However, the bidirectional solution is unstable [22, 23]. We thus focus on the unidirectional solutions $A_+^{st} \neq 0$ and $A_-^{st} = 0$ without loss of generality (the counter-propagating solution can be directly obtained by replacing + with − in the final results). Using (14) in (13) and solving the resulting differential equation, we find

$$A_+^{st}(s) = A_+^{st}(0)e^{i\widetilde{\omega}s + \frac{g}{1+i(\widetilde{\delta}-\widetilde{\omega}/\gamma)}G(s)}, \qquad (17)$$

where

$$G(s) = \int_0^s D_0^{st}(s')ds'. \qquad (18)$$

We note that $D_0^{st} = \frac{dG(s)}{ds}$, hence using (14) and (17) in (15) yields

$$\frac{dG}{ds} = \frac{J}{1+\frac{2g}{1+(\widetilde{\delta}-\widetilde{\omega}/\gamma)^2}|A_+(0)|^2 e^{\frac{2g}{1+(\widetilde{\delta}-\widetilde{\omega}/\gamma)^2}G(s)}}\,. \qquad (19)$$

Clearly, $G(s = 0) = 0$, and the boundary condition for the field $A_+^{st}(0) = tA_+^{st}(1)$ imposes that

$$G(1) = \frac{-\ln t}{g}[1 + (\widetilde{\delta} - \widetilde{\omega}/\gamma)^2], \qquad (20)$$

$$\widetilde{\omega} = \frac{2\pi m - \widetilde{\delta}\ln t}{1 - \frac{\ln t}{\gamma}}. \qquad (21)$$

We note that (21) is equivalent to (9) in this simplified case. Integrating (19) from one end to the other of the laser cavity and using the boundary conditions for $G(s)$ allows us to determine

$$|A_+^{st}(0)|^2 = \frac{J + \frac{\ln t}{g}[1 + (\widetilde{\delta} - \widetilde{\omega}/\gamma)^2]}{e^{-2\ln t} - 1} \,. \qquad (22)$$

We can therefore solve for $G(s)$ and determine the intensity profile of the field along the laser cavity as shown in Fig. 3.

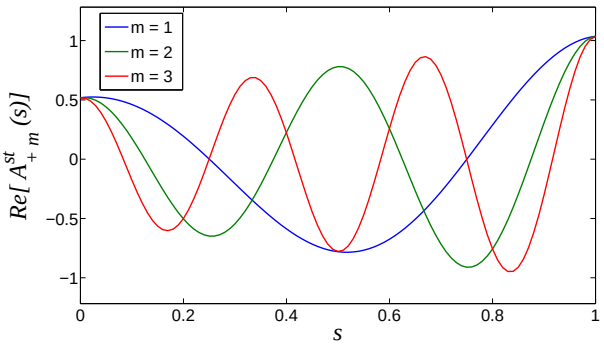

FIG. 3: Re$[A_{+m}^{st}(s)]$ in the unidirectional solution. $\widetilde{\delta} = 0.1$, $g = 1$, $t = 0.5$, $\gamma = 100$ and $J = 1.5$.

The physical insight gained in the analysis of the simplest case suggests that in general, eqs. (13-16) can be very efficiently solved by means of a numerical shooting method [24] which is useful since no analytical solution is possible in this case. In Fig. 4 a bidirectional monochromatic solution calculated in this way is shown. This shooting method can be used to quickly find the

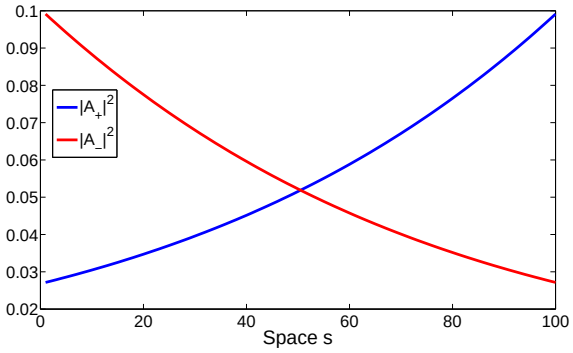

FIG. 4: Bidirectional Monochromatic solutions in the general case. Intensity of the fields inside the cavity vs space s. Mesh points $N = 100$, $J = 0.5$, $\widetilde{\delta} = 0.1$, $g = 1$, $\epsilon = \eta = 10^{-2}$, $\beta = 0$, $t = 0.5$, $r = 2\ 10^{-2}$, $\alpha = 0$ and $\gamma = 100$.

steady state solutions for different current values, hence limited bifurcation diagrams as a function of the pump can be readily obtained. For instance, Fig. 5 depicts the pitchfork bifurcation from a bidirectional solution into two degenerate, almost unidirectional solutions that has been observed in different ring laser systems [5]. It should be noted that, in order to obtain a bifurcation diagram like that in Fig. 5, it is necessary to perform a double scan, one upwards and one downwards, since the shooting method follows the resulting branches even if they are unstable.

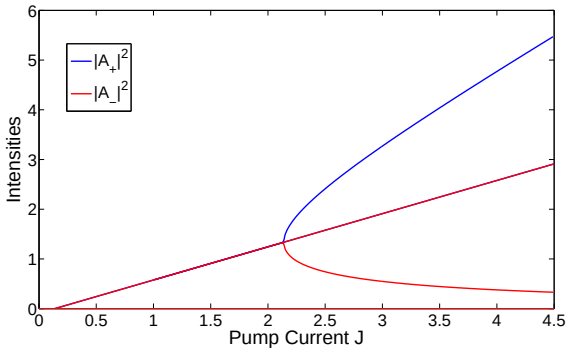

FIG. 5: Bifurcation diagram of the monochromatic solutions: for decreasing pump J showing a pitchfork bifurcation and for increasing J showing a bidirectional solution and the off solution. Mesh points $N = 100$, $\widetilde{\delta} = 0$, $g = 5$, $\epsilon = 10^{-2}$, $\eta = 5$, $\beta = 0$, $t = 0.5$, $r = 5\ 10^{-3}$, $\alpha = 0$ and $\gamma = 100$.

III. TEST: SINGLE-MODE DYNAMICS

The numerical implementation of partial-differential equations always represents a challenge from a technical point of view. In particular, the usual numerical diffusion present in most algorithms has to be carefully taken care off. While numerical dissipation can be helpful in context like e. g. fluid mechanics, to prevent spurious solutions to rise, multi-mode laser dynamics is mainly governed by extremely weak gain difference between consecutive modes that correspond to increasing spatial frequencies. Any weak numerical dissipation would therefore profoundly affect the dynamical scenario and has to be avoided. To this purpose we employ a numerical algorithm that is based on the one presented in [17], which takes advantage of the fact that the equations for the electric fields can be formally solved by integration along the characteristics.

In this section we discuss the tests performed in order to check the correctness and accuracy of the numerical algorithm used to implement the TWM, which is required for controlling potential implementation mistakes. The details of the numerical implementation are described in appendix B, where we also discuss in detail how the boundary conditions are imposed.

Clearly, the results in II.A and II.B provide a first test of the accuracy of the numerical implementation. We have verified that our numerical scheme accurately recovers the lasing threshold yielding monochromatic solutions that match those obtained by the shooting method.

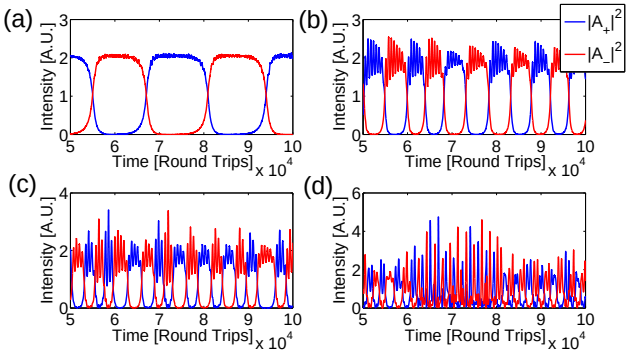

FIG. 6: Dynamical behaviors observed for fixed pump $J = 0.5$ while scanning detuning $\widetilde{\delta}$. (a) $\widetilde{\delta} = 0.2$, (b) $\widetilde{\delta} = 0.5$, (c) $\widetilde{\delta} = 0.7$, (d) $\widetilde{\delta} = 0.9$. The parameters correspond to those used in [25] in Figs. 10a - 10i except for the fact that in our case the two modes have equal losses: Mesh points $N = 100$, $g = 1$, $\epsilon = \eta = 1.78\ 10^{-5}$, $\beta = 10^{-4}$, $t = 0.9$, $r = 0$, $\alpha = 0$ and $\gamma = 1$.

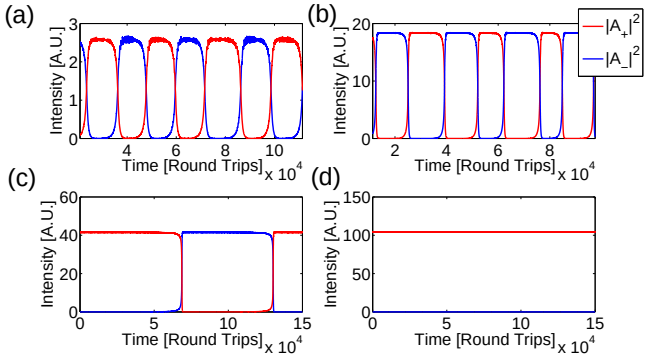

FIG. 7: Dynamical behaviors obtained for fixed detuning $\widetilde{\delta} = 0.2$ while scanning J. (a) $J = 0.6$, (b) $J = 3.6$, (c) $J = 8$, (d) $J = 20$ for the same parameters as in Fig. 6.

A further test, presented below, is provided by comparing our numerical results in the single longitudinal mode limit with the dynamical results previously obtained by Zeghlache et al. [25] with a rate equation model for a CO_2 ring laser. In such a model, obtained in the good cavity limit for a pure single-longitudinal ring laser ($r = 0$), the only term that mixes the counter-propagating fields is the carrier grating, hence the bidirectional regime is unstable [22, 23]. Moreover, the analysis performed in [25] demonstrates that the unidirectional solution can also become unstable in some pump and detuning regimes. For certain values of these parameters, square-wave oscillations between the counter-propagating fields appear followed by regular or even chaotic oscillations. Scanning the pump J for fixed detuning, the system, which is initially stable or bistable, becomes unstable at a certain value, and it eventually recovers stability at high pump values; for fixed pump, instead, stable behavior is not recovered upon increasing detuning although it must be recalled that the single-mode approximation will eventually break down and the model in [25] be no longer valid.

A meaningful comparison of our results from those in [25] requires to establish the equivalence among the parameters in both models. In order to do so, we reduce our model to that in [25] by neglecting any spatial dependence while redefining the losses in (1) as $\alpha_T = \alpha - \ln t$ (i. e., the total losses). Then, comparison with eqs. (3.11) in [25] yields the parameter correspondence rules

$$d_{\parallel} = \frac{\epsilon}{\alpha_T},\ A = \frac{gJ}{\alpha_T},\ \Delta = -\widetilde{\delta}. \tag{23}$$

Our numerical simulations reproduce accurately the behaviors described in [25]. We perform simulations fixing the pump and increasing the detuning (see Fig. 6), in this case, we go from the unidirectional steady emission to a region of instability where the counter-propagating fields develop a square-wave oscillation with one intensity in anti-phase with the other (Fig. 6 (a)). Increasing the detuning the square-waves become distorted and a secondary oscillation appears (Fig. 6 (b) and (c)), progressing until a chaotic oscillation is obtained for high detunings as shown in Fig. 6 (d).

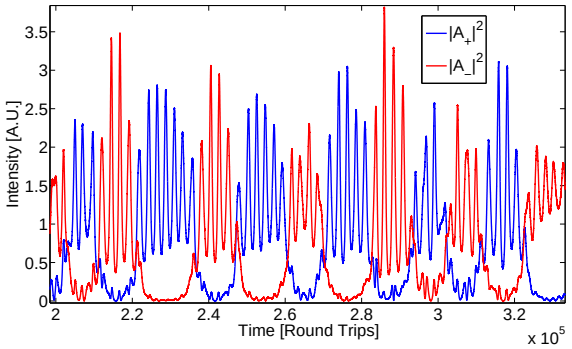

FIG. 8: Single mode chaotic behavior. Mesh points $N = 100$, $J = 0.4$, $\widetilde{\delta} = 0.4$, $g = 1$, $\epsilon = \eta = 1.78\ 10^{-5}$, $\beta = 10^{-4}$, $t = 0.9$, $r = 5\ 10^{-4}$, $\alpha = 0$ and $\gamma = 1$.

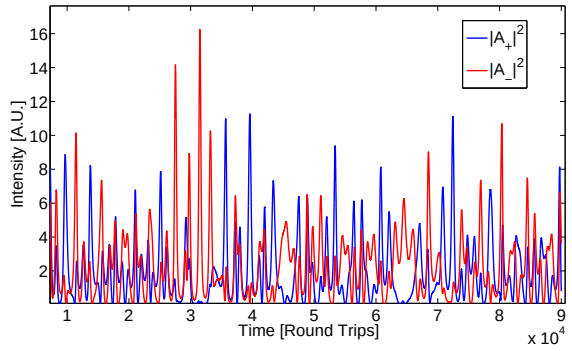

FIG. 9: Single mode chaotic behavior. Mesh points $N = 100$, $J = 0.5$, $\widetilde{\delta} = 1$, $g = 1$, $\epsilon = \eta = 1.78\ 10^{-5}$, $\beta = 10^{-4}$, $t = 0.9$, $r = 5\ 10^{-4}$, $\alpha = 0$ and $\gamma = 1$.

On the other hand, when we fix the detuning and scan the pump (see Fig. 7) we pass from a unidirectional steady solution near threshold into a region of instability where square-waves similar to those in the previous case developed. In contrast with the previous case, now the system recovers stability upon increasing J and returns to one of the unidirectional solutions. The mechanism is a slowing down of the square-wave modulation as we increase the pump (see Fig. 7 (c)), a characteristic behavior of heteroclinic bifurcations.

Finally, we remark that the above behaviors are recovered even when putting a small reflection and spontaneous emission provided that the good cavity limit still applies (see Fig. 8 and 9), i. e., they are robust against small imperfections and noise. However, if the reflectivity is too large, the system emits bidirectionally at threshold and its dynamical behavior is no longer the same [5, 7].

IV. MULTI-MODE DYNAMICS

The RE model described in [25] is of limited applicability because in a real laser, increasing the detuning will eventually lead to at least a change in lasing mode which is not accounted for in the RE model. Indeed, the maximum allowed detuning in a real device corresponds to having the gain peak just between two laser modes, i. e., $\widetilde{\delta} = \pi/\gamma$ in our parametrization. In addition, instabilities arising from the multi-mode character of the system as e. g. the Risken-Nummedal instability [26] can develop when the gain curve is broader than the mode spacing.

The dynamics in these cases can readily be analyzed with the travelling wave model, which naturally retains the dynamics of the different modes and the effects of the detuning. Hence it can allow to explore the dynamics of the system in cases where different longitudinal modes are active.

In this section we present and discuss some remarkable dynamical behaviors obtained in these situations, although we note that the large variety of behaviors that we have observed calls for the development of a bifurcation tool of our TWM that would allows to better understand the role played by the different parameters. To the best of our knowledge, these results have not been found in literature. It should be noted, however, that some of them are obtained for very high pumping levels, $J \sim 10 - 100 J_{th}$, which might be difficult or even impossible to achieve in an experiment. First, we present the situation where a moderate gain bandwidth is taken into account, and how different behaviors arise in this case depending on the pump and the detuning. In the second part of this section the case of a large gain bandwidth is discussed.

A. Moderate gain bandwidth

We consider here the case when the gain spectrum has moderate width, $\gamma = 10$. We first discuss the case when the gain spectrum peak lies just between two modes, $\widetilde{\delta} = 0.3141$. In this case, modes $m = 0$ and $m = 1$ have exactly the same threshold, so the dynamical scenario at the laser threshold corresponds to a degenerate Hopf bifurcation. It should moreover be noted that for each of these frequencies there are two different solution branches which for small r are also almost degenerate, as discussed in II.A. This highly degenerated situation allows the system to lase in a great variety of possible states, which can give rise to unexpected dynamical behaviors. We subsequently discuss the effect of the detuning in this case, since varying the detuning allows to reduce the degeneracy of the system.

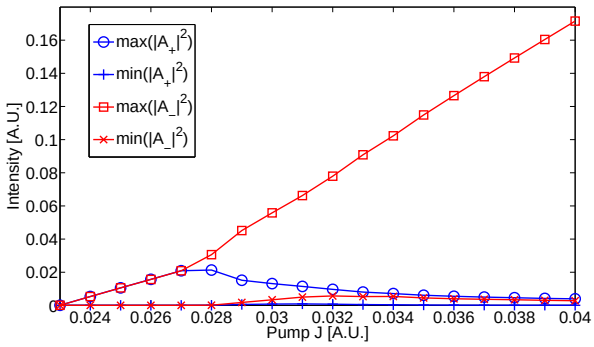

FIG. 10: Bifurcation diagram near threshold. The fields begin to emit multi-mode bidirectionally, then after $J = 0.028$ the backward (-) field is favored. Mesh points $N = 100$, $\widetilde{\delta} = 0.3141$, $g = 5$, $\epsilon = 10^{-2}$, $\eta = 0.1$, $\beta = 10^{-4}$, $t = 0.9$, $r = 5\ 10^{-4}$, $\alpha = 0$ and $\gamma = 10$

Fig. 10 shows the bifurcation diagram near the threshold for the ring laser with moderate gain bandwidth (laser parameters specified in the caption). First, the two counter-propagating fields are both emitting with equal intensity in two modes separated by one mode spacing, i.e. the laser starts to emit bidirectionally in consecutive modes, $m = 0$ and $m = 1$. As we increase the pump, one of the directions becomes dominant over the other, and additional modes are excited. For high enough pump (see Fig. 11), the system emits almost unidirectionally; however, the emission exhibits 100% oscillations at the roundtrip time which correspond to an emission spectrum that involves four dominant modes. Further increasing the pump, the intensity oscillation becomes nonlinear, which corresponds to the locking of a moderate number of modes (see Fig. 12), this regime can be interpreted as a shallow mode-locked solution.

At even higher pumps, the nonlinear oscillation disappears and the emission becomes again bidirectional with both directions emitting stable and with the same power (see Fig. 13).

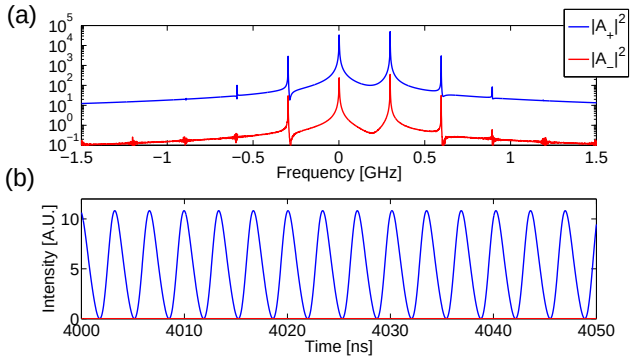

FIG. 11: Unidirectional oscillating emission. (a) Power spectra. (b) Time trace. Mesh points $N = 400$, $J = 1$, $\widetilde{\delta} = 0.3141$, $g = 5$, $\epsilon = 10^{-2}$, $\eta = 0.1$, $\beta = 10^{-4}$, $t = 0.9$, $r = 5\ 10^{-4}$, $\alpha = 0$, $\gamma = 10$, $n = 1$ and $L = 1\ m$.

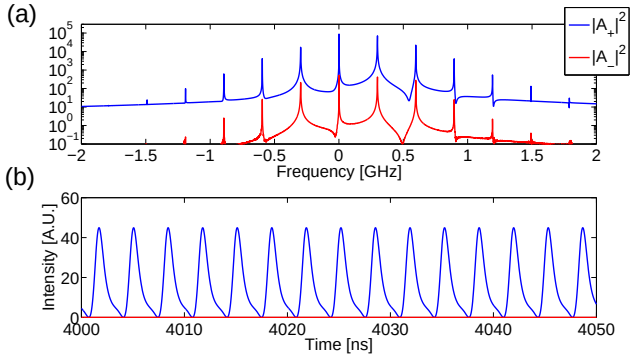

FIG. 12: Mode-locked solution. (a) Power spectra. (b) Time trace. $J = 3$. Other parameters see Fig. 11.

However, a closer look at the emission in this regime (see Fig. 14) reveals that, surprisingly, each emission direction is dominated by a single mode, $m = 0$ for A_+ and $m = 1$ for A_-. Hence each mode contributes in complementary ways to lasing in each direction: while emission in the forward direction is dominated by the redmost mode, the backward direction lases dominantly on the bluest mode. This regime is of course two fold degenerate. This transition comes from the dynamical effect in the population inversion grating. This grating is known to favors unidirectional emission since it cross saturate the forward and backward amplitudes. However, when the forward and backward modes are separated apart in lasing frequency, the efficiency of the grating is strongly decreased since it has to follow the beatnote at the modal separation. As a consequence, while the system cannot emit bidirectionally in the same mode [22, 23] due to too strong a cross saturation, it is still possible to do so when the energy is mainly distributed between two consecutive modes for which the grating effect is strongly mitigated. Decreasing the pump this regime survives and the oscillations do not appear (see Fig. 13), this fact allow us to conclude that we are in a bistable situation.

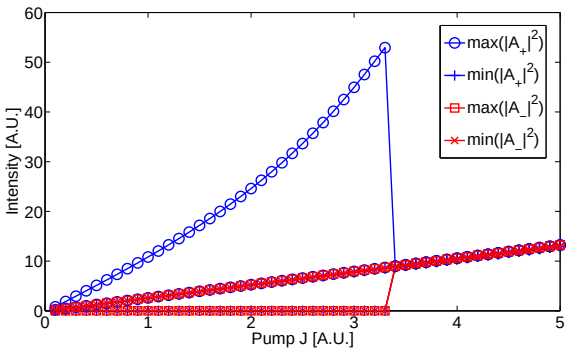

FIG. 13: Bifurcation diagram showing the transition from unidirectional oscillating emission to bidirectional emission at different frequencies while increasing the pump J. Decreasing the pump the system emits bidirectionally at different frequencies. (a) Power spectra. (b) Time trace. Mesh points $N = 400$, $\widetilde{\delta} = 0.3141$, $g = 5$, $\epsilon = 10^{-2}$, $\eta = 0.1$, $\beta = 10^{-4}$, $t = 0.9$, $r = 5\ 10^{-4}$, $\alpha = 0$ and $\gamma = 10$.

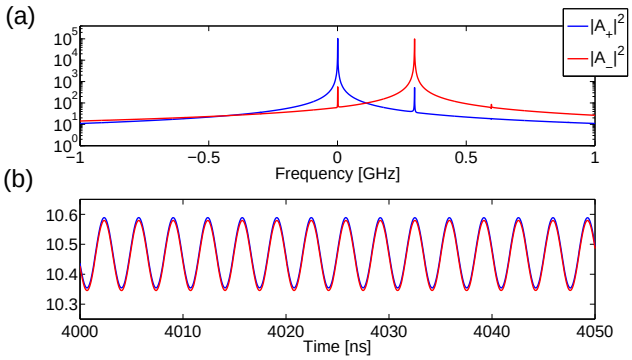

FIG. 14: Bidirectional oscillating emission at different frequencies. (a) Power spectra. (b) Time trace. $J = 4$. Other parameters see fig.11.

1. *Dependence on detuning*

In order to see the effect of the detuning on the behavior of the laser in the case of moderate gain bandwidth, we perform simulations for different $\widetilde{\delta}$. For $\widetilde{\delta} = 0.3$, the laser begins to emit bidirectionally in a mode $m = 0$ but it rapidly becomes almost unidirectional with a small amplitude oscillation that corresponds to residual emission in mode $m = 1$ (see inset in Fig. 15). As we increase the pump, the emission becomes increasingly unidirectional and single mode until $J = 0.4$, where mode $m = 1$ starts to lase and favors the opposite direction. Above this pump value, the laser emits bidirectionally with each direction dominated by a different mode as in the previous subsection. However, the non symmetrical position of the cavity modes with respect to the peak of the gain curve produces a sensible difference between the intensities of the two counter-propagating fields (see Fig. 16).

The above results have been obtained by starting the

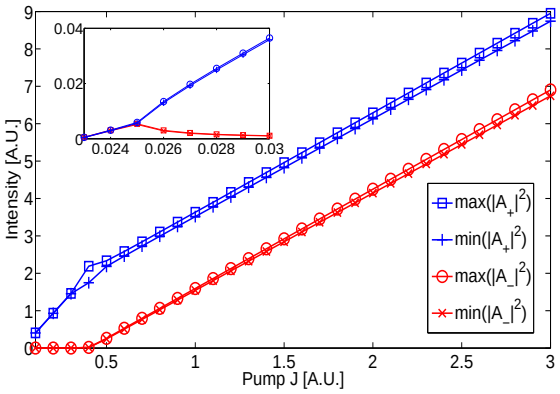

FIG. 15: Bifurcation diagram for $\gamma = 10$ and $\widetilde{\delta} = 0.3$. Inset: Bifurcation diagram near the threshold. Mesh points $N = 400$, $g = 5$, $\epsilon = 10^{-2}$, $\eta = 0.1$, $\beta = 10^{-4}$, $t = 0.9$, $r = 5\ 10^{-4}$ and $\alpha = 0$.

simulations from a noisy initial condition that does not favor any of the emission directions. However, when the simulations are launched from an initial condition that privileges one of the directions (see Fig. 17), we find for some current values an almost unidirectional solution oscillating at the modal beat note with almost 100% amplitude. This solution is the analogous to that in Fig. 13 in the previous subsection, and it eventually also disappears into the bidirectional solution of Fig. 15. The former result evidences that the unidirectional oscillating solution and the bidirectional emission at different frequencies can coexist depending on the parameters. We have tried to induce jumps among these two types of solutions by injecting optical pulses, but we have not managed to stably control the emission state of the system: after a relatively long transient, the system returned to the original emission state, indicating that in spite of their coexistence, the perturbation in phase space requires specific characteristics to place the system into the basin of attraction of the other solution.

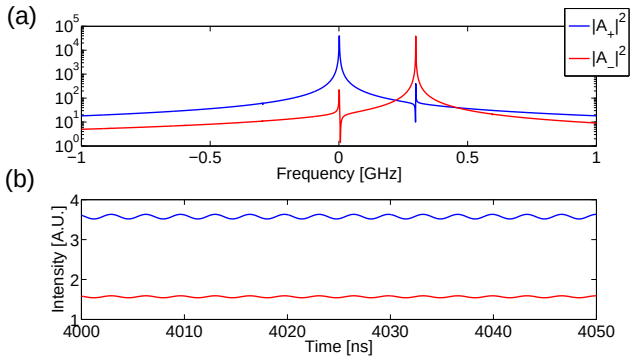

FIG. 16: Bidirectional emission. (a) Power spectra. (b) Time trace. Mesh points $N = 400$, $J = 1$, $\widetilde{\delta} = 0.3$, $g = 5$, $\epsilon = 10^{-2}$, $\eta = 0.1$, $\beta = 10^{-4}$, $t = 0.9$, $r = 5\ 10^{-4}$, $\alpha = 0$, $\gamma = 10$, $n = 1$ and $L = 1\ m$.

Finally, in the case where the gain peak is close to one of the cavity modes, multi-mode dynamics is suppressed because the mode closest to the gain peak takes all the energy provided to the system. For a detuning value $\widetilde{\delta} = 0.15$ the laser emits single-mode unidirectionally as shown in Fig. 18.

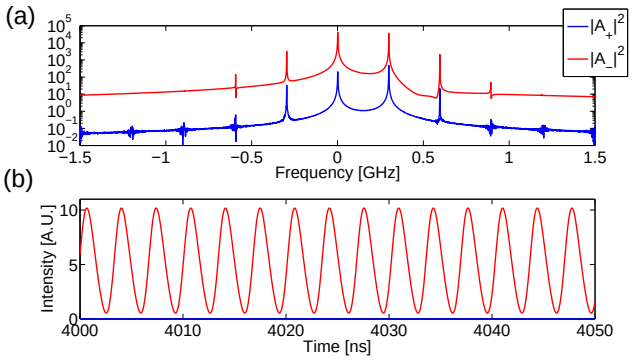

FIG. 17: Unidirectional oscillating emission. (a) Power spectra. (b) Time trace. For parameters see Fig. 16.

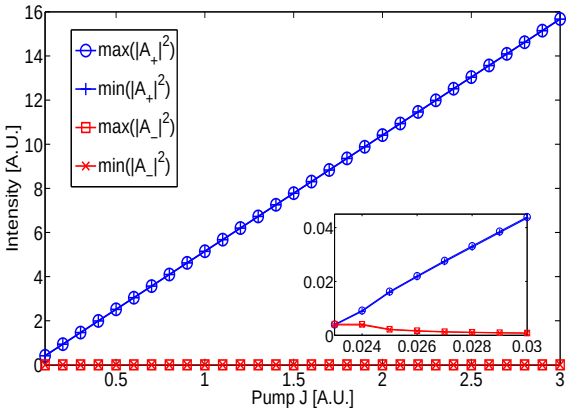

FIG. 18: Bifurcation diagram for $\gamma = 10$ and $\widetilde{\delta} = 0.15$. Inset: Bifurcation diagram near the threshold. Mesh points $N = 400$, $g = 5$, $\epsilon = 10^{-2}$, $\eta = 0.1$, $\beta = 10^{-4}$, $t = 0.9$, $r = 5\ 10^{-4}$ and $\alpha = 0$.

B. Large gain bandwidth

In this section we consider a large gain bandwidth ($\gamma = 100$) that allows for a rich variety of dynamical behaviors because a large number of modes can become active.

The bifurcation diagram shown in Fig. 19 summarizes the different behaviors observed when the peak of the gain curve is just between the first two modes, $\widetilde{\delta} = 0.03141$. Close to threshold, the laser emits bidirectionally with two modes active in each direction as in Fig. 10. Increasing the pump, the forward direction becomes dominant and mode $m = 0$ dominates; conversely,

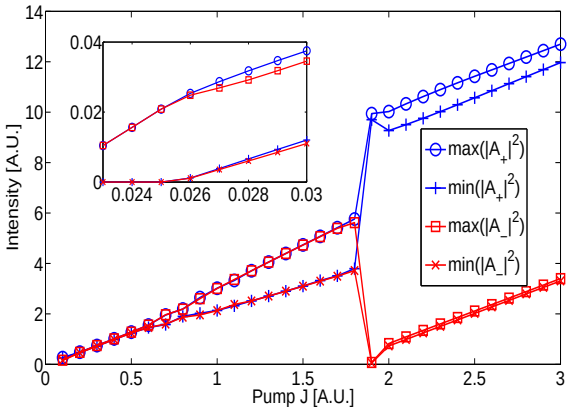

FIG. 19: Bifurcation diagram showing different behaviors for $\gamma = 100$ and $\widetilde{\delta} = 0.03141$. Inset: Bifurcation diagram near the threshold. First, close to threshold, the laser emits bidirectionally with both counter-propagating fields emitting at 2 consecutive modes. Then a regime of bidirectional emission at different frequencies appears (see Fig. 20). Third, a oscillating regime where the counter-propagating fields are out of phase (see Fig. 21). Fourth, a unidirectional multi-mode solution, composed by not consecutive modes (see Fig. 22). Fifth, a bidirectional emission at different frequencies at not consecutive modes (see Fig. 23). Mesh points $N = 400$, $g = 5$, $\epsilon = 10^{-2}$, $\eta = 2\ 10^{-2}$, $\beta = 10^{-4}$, $t = 0.9$, $r = 5\ 10^{-4}$ and $\alpha = 0$.

the backwards direction is dominated by mode $m = 1$ (see Fig. 20). In this regime, both emission directions oscillate in phase, but as the pump is still increased, more modes become excited and the oscillations of the intensity of the counter-propagating fields are out of phase (see Fig. 21).

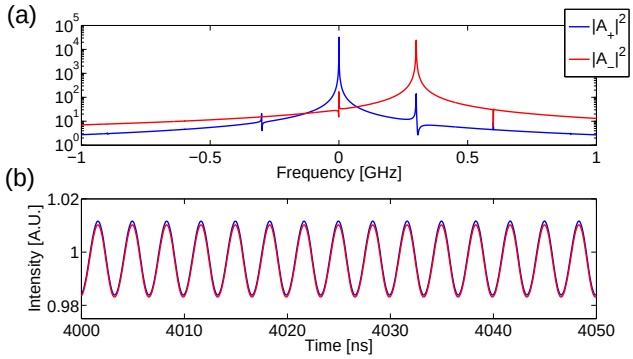

FIG. 20: Bidirectional emission at different frequencies. (a) Power spectra. (b) Time trace. Mesh points $N = 400$, $J = 0.4$, $\widetilde{\delta} = 0.03141$, $g = 5$, $\epsilon = 10^{-2}$, $\eta = 2\ 10^{-2}$, $\beta = 10^{-4}$, $t = 0.9$, $r = 5\ 10^{-4}$, $\alpha = 0$, $\gamma = 100$, $n = 1$ and $L = 1\ m$.

Still increasing the pump, a regime of almost single-mode, unidirectional emission is recovered (see Fig. 22) for a small range of pump values. We see that in this case, the depressed emission direction is dominated by mode

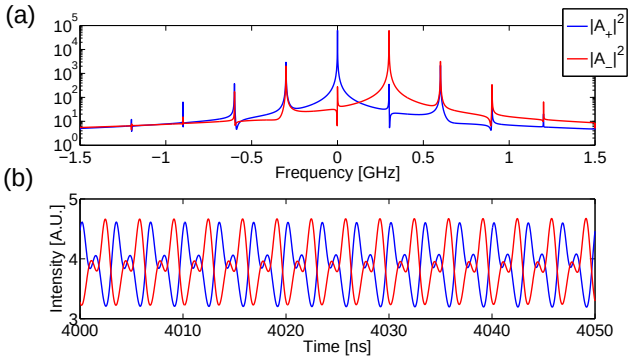

FIG. 21: Multi-mode alternate oscillations. (a) Power spectra. (b) Time trace. $J = 1.5$. Other parameters see Fig. 20.

$m = 2$, with a secondary peak on mode $m = -2$ excited by Four-Wave-Mixing processes. Such a regime indicates that the gain suppression of mode $m = 1$ by emission on mode $m = 0$ is strong enough to inhibit emission on mode $m = 1$. However, the large bandwidth of the gain curve allows modes farther away from mode $m = 0$ to become active when the pump is still increased. As shown in Fig. 23, this leads again to a bidirectional solution where each direction dominantly lases on different modes separated by twice the mode spacing.

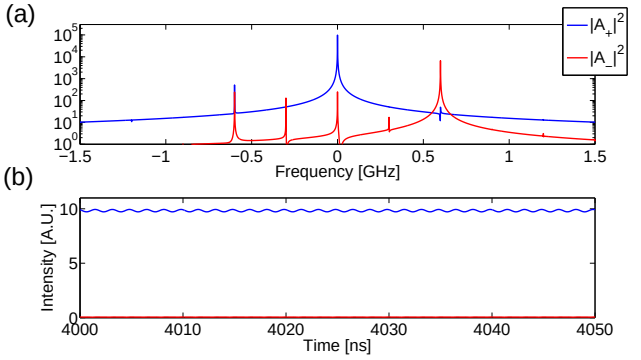

FIG. 22: Unidirectional emission. (a) Power spectra. (b) Time trace. $J = 1.9$. Other parameters see Fig. 20.

1. *Dependence on detuning*

For detuning values above $\widetilde{\delta} = 0.025$, the behavior of the system is qualitatively the same described in the previous subsection (see Fig. 24). However, the non symmetrical position of the gain curve peak makes the DC component of the fields different and a unidirectional solution is found near threshold.

A different scenario emerges at low detunings. When the detuning is decreased to a value $\widetilde{\delta} = 0.015$ (see Fig. 25), the laser starts emitting bidirectionally with both directions emitting on two consecutive modes. For

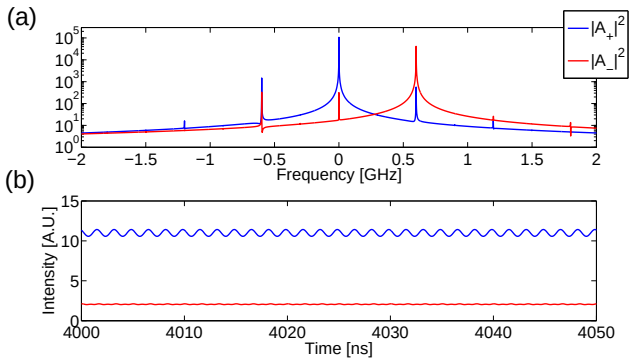

FIG. 23: Bidirectional emission at different frequencies. (a) Power spectra. (b) Time trace. $J = 2.5$. Other parameters see Fig. 20.

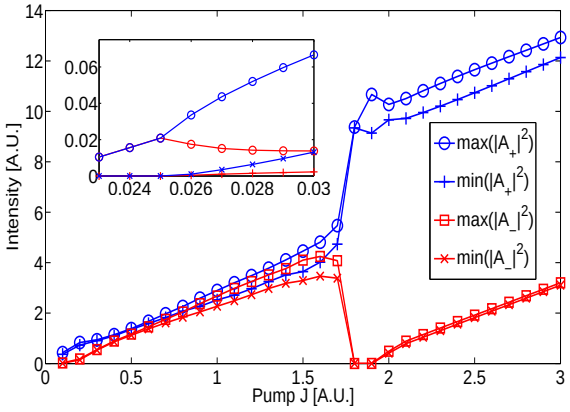

FIG. 24: Bifurcation diagram for $\gamma = 100$ and $\widetilde{\delta} = 0.03$. Inset: Bifurcation diagram near the threshold. First, bidirectional emission is found near threshold, then one of the fields is suppressed and a unidirectional regime is found, after that the suppressed field begins to emit at a different frequency respect to the emitted by the no suppressed field and a bidirectional solution appears. Increasing the pump we find a unidirectional solution that end up in a bidirectional solution emitting at not consecutive modes. Mesh points $N = 400$, $g = 5$, $\epsilon = 10^{-2}$, $\eta = 2\ 10^{-2}$, $\beta = 10^{-4}$, $t = 0.9$, $r = 5\ 10^{-4}$ and $\alpha = 0$.

slightly higher pump, one emission direction starts to dominate with quasi single-mode emission up to $J \approx 2.4$, where a unidirectional solution arises with a high number of active modes (see Fig. 26). Although this solution appears very far away from the lasing threshold, it is worth being examined in detail. The solution has the characteristics of a mode-locked state, with sharp and narrow ($\approx 0.2\ ns$ full-width at half-maximum) pulses being emitted in one direction only. Since the roundtrip time in our case corresponds to 3.3 ns, the duty-cycle of the pulses is around 6%. It is worth remarking that this solution appears without inserting in the cavity any additional element that favors pulsed operation (i. e., a saturable absorber or alike), but it merely arises from an instability of the CW solution occurring when the power level is such that the Rabi frequency of the two-level atoms equals the polarization dephasing rate. From this point of view, then, the mechanism that triggers this solution is analogous to that in the Risken-Nummedal instability. The main difference between our case and the classical Risken-Nummedal instability is that the large gain curve that we are considering allows for the excitation of additional side-modes through Four-Wave Mixing processes mediated by both D_0 and $D_{\pm 2}$, which give rise to the pulsed emission of the system.

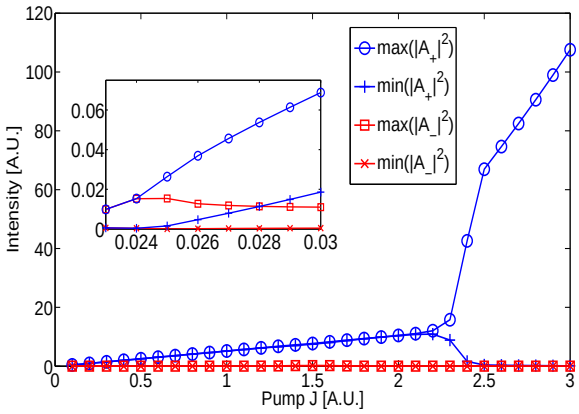

FIG. 25: Bifurcation diagram for $\gamma = 100$ and $\widetilde{\delta} = 0.015$. Inset: Bifurcation diagram near the threshold. Near threshold the laser emits bidirectionally but for a wide range on pump the laser emits unidirectionally single-mode, then near $J = 2.2$ different modes start to lase and a mode-locked solution arises (see Fig. 26). Mesh points $N = 400$, $g = 5$, $\epsilon = 10^{-2}$, $\eta = 2\ 10^{-2}$, $\beta = 10^{-4}$, $t = 0.9$, $r = 5\ 10^{-4}$ and $\alpha = 0$.

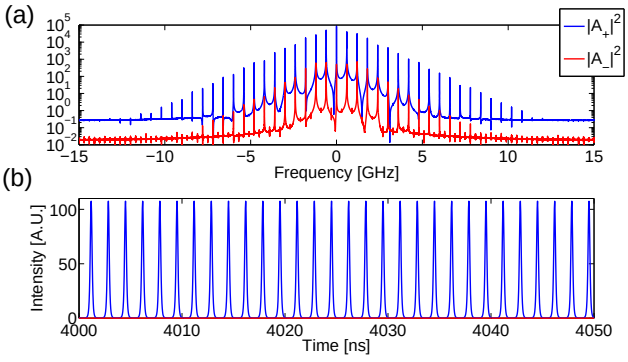

FIG. 26: Mode-locked emission. (a) Power spectra. (b) Time trace. Mesh points $N = 400$, $J = 3$, $\widetilde{\delta} = 0.015$, $g = 5$, $\epsilon = 10^{-2}$, $\eta = 2\ 10^{-2}$, $\beta = 10^{-4}$, $t = 0.9$, $r = 5\ 10^{-4}$, $\alpha = 0$, $\gamma = 100$, $n = 1$ and $L = 1\ m$.

V. CONCLUSIONS

The multi-mode dynamics of a two-level ring laser has been explored using a bidirectional TWM. The model and its numerical implementation have been tested by reproducing the dynamical results obtained in the single-mode limit by Zeghlache et al. [25] We have shown that the dynamical regimes reported in [25] are robust against noise and residual reflections provided that the single-mode limit holds. We have found novel dynamical regimes where the emission in each direction occurs at different wavelengths, each direction being associated to a different longitudinal mode. In addition, the influence of the detuning and the width of the gain spectrum have been thoroughly analyzed, and the onset of unidirectional, mode-locked emission for large gain bandwidth and relatively small detuning has been studied in detail.

APPENDIX A: DERIVATION OF THE MODEL

The wave equation for a electric field $\mathcal{E}(z,t)$ in a medium can be written as

$$\frac{\partial^2\mathcal{E}}{\partial z^2}-\frac{n^2}{c^2}\frac{\partial^2\mathcal{E}}{\partial t^2}=\mu\frac{\partial^2\mathcal{P}}{\partial t^2}, \tag{A1}$$

where $\mathcal{P}$ is the polarization of the medium, n is the refraction index of the medium, c is the speed of light in vacuum and μ is the magnetic permeability of the medium [19, 27]. If we suppose that the field is quasi-monochromatic and decomposed into forward (+) and backward (-) propagation directions, $\mathcal{E}(z,t)$ takes the form

$$\mathcal{E}(z,t)=[E_+(z,t)e^{iq_0z}+E_-(z,t)e^{-iq_0z}]e^{-i\omega_0t}+c.c., \tag{A2}$$

where $c.c.$ denotes complex conjugate and $E_\pm(z,t)$ is slowly varying both in space and time, as compared with q_0^{-1} and ω_0^{-1}, respectively. In the same way we consider quasi-resonant light-matter interaction in the RWA, then the total polarization exhibits only a frequency component ω_0 and is decomposed into forward and backward propagation directions, it reads as

$$\mathcal{P}(z,t)=i\{[P_+(z,t)e^{iq_0z}+P_-(z,t)e^{-iq_0z}]e^{-i\omega_0t}-c.c.\}. \tag{A3}$$

Using these assumptions we can write the slowly varying approximation (SVA) [19] for the wave equation (A1) as

$$\pm\frac{\partial E_\pm}{\partial z}+\frac{n}{c}\frac{\partial E_\pm}{\partial t}=-\frac{\omega_0c\mu}{2n}P_\pm. \tag{A4}$$

These equations are complemented with boundary conditions [28] for the geometry considered, in this case a ring, that can be written as

$$\begin{aligned}E_+(0) &= t_+E_+(L)e^{iq_0L}+r_-E_-(0),\\ E_-(L)e^{-iq_0L} &= t_-E_-(0)+r_+E_+(L)e^{iq_0L},\end{aligned} \tag{A5}$$

where L is the length of the ring and $t_\pm$ and $r_\pm$ denote the transmissivity and reflectivity of the forward and backward waves, which follows $|t_\pm|^2+|r_\pm|^2=1-\varepsilon_\pm$, where $\varepsilon_\pm$ are the losses at the point coupler.

The medium assumed is composed of N identical two level atoms per unit volume, with a resonance frequency ω_A between the upper and the lower levels. As one can find in the literature [19, 27] these features lead to a pair of equations, one to describe the population difference dynamics and another equation to describe the polarization dynamics.

It is known from early studies that the presence of counter-propagating fields creates a spatial modulation of the population inversion. This important property follows from the iterative relationship between the diagonal and off-diagonal matrix elements of the density matrix $\hat{\rho}$ [29]. As a result only odd harmonics appear in the expansion of $\mathcal{P}$ and only even harmonics appear in the expansion of the population difference D. This spatial modulation acts as a Bragg grating and creates a coupling between the counter-propagating fields. In order to get the dynamics of this grating explicitly we decompose the population difference in different spatial contributions as

$$D=D_0+D_{+2}e^{2iq_0z}+D_{-2}e^{-2iq_0z}+\dots \tag{A6}$$

Such a decomposition yields an infinite hierarchy of equations that has to be truncated in order to keep the problem treatable. In systems with large diffusion, the truncation can be justified due to the quadratically increasing damping of the high-order terms [18, 20]; in other cases, the intensity of the fields has to be low compared to the saturation intensity of the medium [25]. Using the decomposition of the fields and the polarization in their propagation directions and the decomposition of the population difference in the spatial contributions we obtain the equations to describe the medium,

$$\frac{\partial P_\pm}{\partial t}=-(i\delta+\gamma_\perp)P_\pm-\frac{\widetilde{\mu}^2}{\hbar}(D_0E_\pm+D_{\pm2}E_\mp), \tag{A7}$$

$$\frac{\partial D_0}{\partial t}=\frac{2}{\hbar}(E_+P_+^*+E_-P_-^*+c.c.)+J-\gamma_\parallel D_0+\mathbb{D}\partial_z^2D_0, \tag{A8}$$

and

$$\frac{\partial D_{\pm2}}{\partial t}=\frac{2}{\hbar}(E_\pm P_\mp^*+E_\mp^*P_\pm)-(\gamma_\parallel+4q_0^2\mathbb{D})D_{\pm2}. \tag{A9}$$

Where δ is the detuning, which takes into account the difference between the atomic transition frequency and the emission frequency, i. e. $\delta=\omega_A-\omega_0$, $\gamma_\perp$ is the polarization decay rate, $\widetilde{\mu}$ is the component of the dipole operator along the direction of the field, $\hbar$ is the Planck's constant, $\gamma_\parallel$ is the population inversion decay rate, J is the pump parameter and $\mathbb{D}$ is the diffusion coefficient.

Eqs. (A4,A7-A9) are equivalent to eqs. (3.4) in [25] with the only difference that we retained the slow spatial

dependence of the fields while the good cavity limit was invoked in [25] in order to work with time-dependent field amplitudes only. In this way, our approach allows for describing multi-mode dynamics that is beyond the scope of [25].

For numerical purposes it is convenient to rewrite eqs. (A4) and (A7)-(A9) in dimensionless form,

$$\pm\frac{\partial A_\pm}{\partial s} + \frac{\partial A_\pm}{\partial \tau} = B_\pm - \alpha A_\pm \ , \tag{A10}$$

$$\frac{1}{\gamma}\frac{\partial B_\pm}{\partial \tau} = -(1+i\widetilde{\delta})B_\pm + g(D_0 A_\pm + D_{\pm 2}A_\mp) + \sqrt{\beta D_0}\ \xi_\pm(s,\tau) \ , \tag{A11}$$

$$\frac{1}{\epsilon}\frac{\partial D_0}{\partial \tau} = J - D_0 + \Delta\frac{\partial^2 D_0}{\partial s^2} - (A_+B_+^* + A_-B_-^* + c.c.), \tag{A12}$$

$$\frac{1}{\eta}\frac{\partial D_{\pm 2}}{\partial \tau} = -D_{\pm 2} - \frac{\epsilon}{\eta}(A_\pm B_\mp^* + A_\mp^* B_\pm) \ , \tag{A13}$$

where we have scaled the fields and polarizations as

$$A_\pm = \sqrt{\frac{4n}{\mu\omega_0 c\hbar\gamma_\parallel L}}E_\pm, \qquad B_\pm = -\sqrt{\frac{\mu\omega_0 c}{n\hbar\gamma_\parallel L}}P_\pm \ , \tag{A14}$$

we have included in eq. (A10) a term modeling the internal losses α for the electric fields, we have defined new dimensionless parameters

$$\begin{array}{c} g = \frac{\mu\omega_0 c\tilde{\mu}^2 L}{2n\hbar\gamma_\perp}, \quad \gamma = \frac{\gamma_\perp nL}{c}, \ \epsilon = \frac{\gamma_\parallel nL}{c}, \\ \eta = \frac{(\gamma_\parallel + 4g_0^2\mathbb{D})nL}{c}, \ \Delta = \frac{\mathbb{D}}{\gamma_\parallel L^2}, \quad \widetilde{\delta} = \frac{\delta}{\gamma_\perp}, \end{array} \tag{A15}$$

and finally we have defined new coordinates

$$\tau = \frac{c}{nL}t, \qquad s = \frac{z}{L}. \tag{A16}$$

In this new reference frame, the general boundary conditions for the fields in the laser read

$$\begin{array}{rcl} A_+(0) & = & t_+A_+(1)e^{i\gamma\widetilde{\omega}_0} + r_-A_-(0), \\ A_-(1)e^{-i\gamma\widetilde{\omega}_0} & = & t_-A_-(0) + r_+A_+(1)e^{i\gamma\widetilde{\omega}_0}, \end{array} \tag{A17}$$

Usually we shall take $\gamma\widetilde{\omega}_0 = 2\pi m$ where $m = 0, \pm 1, \pm 2 \ldots$ then $e^{i\gamma\widetilde{\omega}_0} = 1$ without loss of generality. It means that we take the carrier frequency ω_0 as one of the modes of the cavity.

We note that the effects of diffusion in (A12) are almost negligible because the characteristic length scale of D_0 is 1 (i.e. the cavity length), so that we can set $\Delta = 0$ in (A12). Instead, we should retain it in (A13) because the characteristic length scale in this case is the emission wavelength $\lambda_0 = 2\pi c/\omega_0$.

Finally, spontaneous emission is modeled by including Langevin noise terms $\xi_\pm(s,\tau)$ [18]. They are taken to be Gaussian white noise in space and time with zero mean and correlations $< \xi_\pm(s,\tau)\xi_\pm(s',\tau') >= \delta(\tau-\tau')\delta(s-s')$, and their intensities are proportional to the population density [30].

APPENDIX B: NUMERICAL ALGORITHM

The numerical algorithm used to perform the simulation of the normalized system of equations (1-4) is based in the one presented in [17]. This algorithm takes advantage of the fact that the equations for the fields can be solved formally in terms of integrals of the polarizations. We discretize time with time step h, hence the spatial grid has also discretization step h. All spatial points $n = 1, ..., N$ are internal, with the first and last points located at $h/2$ from the nearest end (see Fig. 27). We denote by X_j^n the value of variable X at time $t = nh$ and gridpoint $s = jh$.

We use the mid-point discretization scheme for the fields [17], so they are updated according to

$$A_{+\ j}^{n+1} = \frac{1-q}{1+q}A_{+\ j-1}^{n} + p(B_{+\ j-1}^{n} + B_{+\ j}^{n+1}), \tag{B1}$$

$$A_{-\ j}^{n+1} = \frac{1-q}{1+q}A_{-\ j+1}^{n} + p(B_{-\ j+1}^{n} + B_{-\ j}^{n+1}), \tag{B2}$$

where $q = \alpha h/2$, $p = (h/2)(1+q)^{-1}$. For the polarizations we have

$$\begin{array}{rcl} B_{\pm\ j}^{n+1} & = & \mu B_{\pm\ j}^{n} + \nu D_{0\ j}^{n+1/2}(A_{\pm\ j}^{n+1} + A_{\pm\ j}^{n}) \\ & + & \nu D_{\pm 2\ j}^{n+1/2}(A_{\mp\ j}^{n+1} + A_{\mp\ j}^{n}) + \sqrt{\beta h D_0}\ \xi_\pm, \end{array} \tag{B3}$$

where $\mu = [1-(\gamma h/2)(1+i\widetilde{\delta})][1+(\gamma h/2)(1+i\widetilde{\delta})]^{-1}$ and $\nu = (gh\gamma/2)[1+(\gamma h/2)(1+i\widetilde{\delta})]^{-1}$, and where we have used the approximation

$$\int_t^{t+\Delta t} D_k(t)A_l(t)dt \simeq \Delta t\ D_k\left(t+\frac{\Delta t}{2}\right)\frac{A_l(t+\Delta t)+A_l(t)}{2}. \tag{B4}$$

At this point we note that eq. (B3) needs the values of the carriers (D_0 and $D_{\pm 2}$) at intermediate time steps, hence we use a temporal grid for the carrier densities which is staggered by half a time step from the fields and polarizations. This is different from the original algorithm in [17], where the carriers are on the same temporal grid than the fields and the polarizations and then interpolation is used to evaluate the carriers at the intermediate times needed in (B1)-(B3). In our case, the finite difference equations for carriers are thus

$$\begin{array}{rcl} D_{0\ j}^{n+3/2} & = & \rho D_{0\ j}^{n+1/2} + \theta J \\ & - & \theta(A_{+\ j}^{n+1}B_{+\ j}^{*\ n+1} + A_{-\ j}^{n+1}B_{-\ j}^{*\ n+1} + c.c.) \end{array} \tag{B5}$$

$$\begin{array}{rcl} D_{\pm 2\ j}^{n+3/2} & = & \rho D_{\pm 2\ j}^{n+1/2}\ , \\ & - & \theta\left(A_{\pm\ j}^{n+1}B_{\mp\ j}^{*\ n+1} + A_{\mp\ j}^{*\ n+1}B_{\pm\ j}^{n+1}\right)\ . \end{array} \tag{B6}$$

where $\rho = \left(1+\frac{\epsilon h}{2}\right)\left(1-\frac{\epsilon h}{2}\right)^{-1}$ and $\theta = \epsilon h\left(1-\frac{\epsilon h}{2}\right)^{-1}$

Boundary Conditions

In order to impose the general boundary conditions (5), we have to consider that the fields propagate during

half a step, then experience partial reflection and transmission and then they propagate for another half a step. In addition, we recall the ring structure of our system hence points $j = 1$ and $j = N$ are connected through the boundary conditions. This procedure for A_+ and A_- is implemented as follows:
Step (1): We use an explicit Euler method to compute the value of the fields just before arriving at boundary by propagating the fields over half a step

$$\begin{array}{rcl} A_{+\ N+1/2}^{\ n+1/2} - (1-q)A_{+\ N}^{\ n} &=& \frac{h}{2}B_{+\ N}^{\ n}, \\ A_{-\ 1/2}^{\ n+1/2} - (1-q)A_{-\ 1}^{\ n} &=& \frac{h}{2}B_{-\ 1}^{\ n}. \end{array} \tag{B7}$$

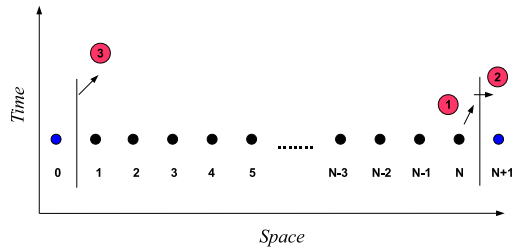

FIG. 27: Schematic representation of spatial discretization and the implementation of the boundary conditions for the A_+ electric field. In three steps: (1) Half step explicit Euler. (2) Boundary Conditions. (3) Half step implicit Euler. The mesh is composed by N points and N intervals and two auxiliar points at 0 and $N+1$ added for the implementation.

Step (2): We apply the boundary conditions and compute the fields just after the boundary, which are denoted as $\widetilde{A}_+$ and $\widetilde{A}_-$

$$\begin{array}{rcl} \widetilde{A}_{+\ 1/2}^{\ n+1/2} &=& t_+ A_{+\ N+1/2}^{\ n+1/2} + r_- A_{-\ 1/2}^{\ n+1/2}, \\ \widetilde{A}_{-\ N+1/2}^{\ n+1/2} &=& t_- A_{-\ 1/2}^{\ n+1/2} + r_+ A_{+\ N+1/2}^{\ n+1/2}. \end{array} \tag{B8}$$

Step (3): Finally we use the implicit Euler method for the remaining half a step to calculate the value of the fields at time $n+1$

$$\begin{array}{rcl} (1+q)A_{+\ 1}^{n+1} - \widetilde{A}_{+\ 1/2}^{n+1/2} &=& \frac{h}{2}B_{+\ 1}^{n+1} \\ (1+q)A_{-\ N}^{n+1} - \widetilde{A}_{-\ N+1/2}^{n+1/2} &=& \frac{h}{2}B_{-\ N}^{n+1} \end{array}. \tag{B9}$$

Note that these procedure can be very efficiently implemented by adding to the spatial grid two auxiliary points $j = 0$ and $j = N+1$ (see Fig. 27) located half a step away from the facets where the fields and polarizations are

$$\begin{array}{rcl} A_{+\ 0}^{\ n} &=& t_+ A_{+\ N}^{\ n} + r_- A_{-\ 1}^{\ n} \\ B_{+\ 0}^{\ n} &=& t_+ B_{+\ N}^{\ n} + r_- B_{-\ 1}^{\ n} \\ A_{-\ N+1}^{\ n} &=& t_- A_{-\ 1}^{\ n} + r_+ A_{+\ N}^{\ n} \\ B_{-\ N+1}^{\ n} &=& t_- B_{-\ 1}^{\ n} + r_+ B_{+\ N}^{\ n} \end{array} \tag{B10}$$

and updating the fields by means of the standard midpoint integration

$$\begin{array}{rcl} A_{+\ 1}^{\ n+1} &=& \frac{1-q}{1+q}A_{+\ 0}^{\ n} + p(B_{+\ 0}^{\ n} + B_{+\ 1}^{\ n+1}), \\ A_{-\ N}^{\ n+1} &=& \frac{1-q}{1+q}A_{-\ N+1}^{\ n} + p(B_{-\ N+1}^{\ n} + B_{-\ N}^{\ n+1}). \end{array} \tag{B11}$$

ACKNOWLEDGMENTS

The authors would like to thank A. Scirè for helpful discussion. This work was partially funded by the european project IOLOS (IST-2005-34743). A.P. thanks the Dept. of Electronics and Electrical Engineering of the University of Glasgow for their hospitality where part of his work was developed. J.J. acknowledges the financial support from EPSRC (project EP-E065112-1). S.B. acknowledges financial support from project BLANCO (PN TEC2006-13887-C05-03).

[1] H. W. Schröder, L. Stein, D. Frölich, B. Fugger and H. Welling, "A High-Power Single-Mode CW Dye Ring Laser", Appl. Phys. **14**, 377 (1977).
[2] M. R. Surette, L. Goldberg and D. Mehuys, "High-Power Ring Laser Using a Broad-Area GaAlAs Amplifier", IEEE Photon. Technol. Lett. **5**, 919 (1993).
[3] X. Donga, H. Tama, B. Guana, C. Zhaoa and X. Dong, "High power erbium-doped fiber ring laser with widely tunable range over 100 nm", Opt. Comm. **224**, 295 (2003).
[4] M. Sorel, A. Scirè, G. Giuliani, R. Miglierina, S. Balle, P.J.R. Laybourn and S. Donati, Opt. Lett. **27**, 1992, (2002).
[5] M. Sorel, G. Giuliani, A. Scirè, R. Miglierina, S. Donati and P.J.R. Laybourn, IEEE J. Quantum Electron. **39**, 1187 (2003).
[6] M. Sorel, P.J.R. Laybourn, G. Giuliani and S. Donati, Appl. Phys. Lett. **80**, 3051 (2002).
[7] C. Born, M. Sorel and S. Yu, IEEE J. Quantum Electron. **41**, 261, (2005).
[8] H. Nakatsuka, S. Asaka, H. Itoh, K. Ikeda and M. Matsuoka, Phys. Rev. Lett. **50**, 109 (1983).
[9] W. W. Chow, J. Gea-Banacloche, L. M. Pedrotti, V. E. Sanders, W. Schleich and M. O. Scully, "The Ring Laser Gyro", Rev. Mod. Phys. **57**, 61 (1985).
[10] M.T. Hill, H.J.S. Dorren, T.de Vrie, X.J.M. Leijtens, J.H. den Besten, B. Smalbrugge, Y.S. Oei, H. Binsma, G.D. Khoe and M.K. Smit, Nature **432**, 206 (2004).
[11] W. E. Lamb, Jr., "Theory of an Optical Maser", Phys. Rev. **134**, A1429 (1964).
[12] F. Aronowitz, "Theory of a Traveling-Wave Optical Maser", Phys. Rev. **139**, A635 (1965).

[13] L. N. Menegozzi and W. E. Lamb, Jr., "Theory of a Ring Laser", Phys. Rev. A **8**, 2103 (1973).
[14] W.R. Christian and L. Mandel, "Frequency dependence of a ring laser with backscattering", Phys. Rev. A **34**, 3932 (1986).
[15] G. Vemuri and R. Roy,"Stochastic resonance in a bistable ring laser", Phys. Rev. A **39**, 4668 (1989).
[16] C. Etrich, P. Mandel, R. Centeno Neelen, R.J.C. Spreeuw and J.P. Woerdman, "Dynamics of a ring-laser gyroscope with backscattering", Phys. Rev. A **46** 525 (1992).
[17] J. A. Fleck, Jr., "Ultrashort-Pulse Generation by Q-Switched Lasers", Phys. Rev. B **1**, 84 (1970)
[18] M. Homar, J. V. Moloney and M. San Miguel, "Traveling Wave Model of a Multimode Fabry-Pérot Laser in Free Running and External Cavity Configurations", IEEE J. Quantum Electron. **32**, 553 (1996).
[19] L. M. Narducci and N. B. Abraham, *Laser Physics and Laser Instabilities*, World Scientific, Singapore (1988).
[20] J. Javaloyes and S. Balle, "Emission Directionality of Semiconductor Ring Lasers: A Travelling-Wave Description", IEEE J. Quantum Electron. **45**, 431 (2009).
[21] S. Fürst, A. Pérez-Serrano, A. Scirè, M. Sorel and S. Balle, Appl. Phys. Lett. **93** 251109 (2008).
[22] P. Mandel and G. P. Agrawal, "Mode Instabilities in Homegeneously Broadened Ring Laser", Opt. Commun. **42**, 269 (1982).
[23] M. Sargent III, "Theory of a multimode quasiequilibrium semiconductor laser", Phys. Rev. A, **48**, 717 (1993).
[24] W. H. Press, S. A. Teukolsky, W. T. Vetterling and B. P. Flannery, *Numerical Recipes, The Art of Scientific Computing, Third Edition*, Cambridge University Press, New York (2007).
[25] H. Zeghlache, P. Mandel, N.B. Abraham, L.M. Hoffer, G.L. Lippi and T. Mello,"Bidirectional ring laser: Stability analysis and time dependent solutions", Phys. Rev. A, **37**, 470 (1988).
[26] H. Risken and H. Nummedal, "Self-Pulsing in Lasers", J. Appl. Phys. **39** 4662 (1968).
[27] A. Yariv, *Quantum Electronics*, Wiley (1989).
[28] A. E. Siegman, *Lasers*, University Science Books, Mill Valley, CA (1986).
[29] S. Haroche and F. Hartmann, "Theory of Saturated-Absorption Line Shapes", Phys. Rev. A **6**, 1280 (1972).
[30] K. Petermann, *Laser Diode Modulation and Noise*, Kluwer Academic Publishers, (1988).